Wang et al. *Microsystems & Nanoengineering* (2025)11:210
https://doi.org/10.1038/s41378-025-01059-2

Microsystems & Nanoengineering
www.nature.com/micronano

ARTICLE

Open Access

Tunable energy transfer in coupled nonlinear MEMS resonators under parametric modulation for enhanced sensor performance

Guijie Wang[1], Shenglin Hou[2], Najib Kacem[3], Lifang Ran[1], Xiaolong Wen[1,2✉] and Ashwin Seshia[2✉]

Abstract

Coherent control of coupled microelectromechanical resonators within the framework of classical nonlinear dynamics is of relevance in fundamental studies and the development of high-performance sensors. Coherent control can be achieved through the parametric modulation of one of the two coupled resonators. However, microelectromechanical resonators are commonly operated in the nonlinear regime, and a thorough description of key phenomena involving parametric modulation of coupled resonators, such as sideband generation and mode splitting, remains limited in this regime. We use a weakly coupled double-ended tuning fork (DETF) resonator under strong parametric modulation to demonstrate tunable energy transfer and mode interactions governed by classical analogs of well-established quantum phenomena. The method uses a red-sideband parametric signal to manipulate the coupling between two adjacent modes dynamically. This approach is theoretically assessed thanks to a nonlinear reduced-order model that takes into account the modal interactions and virtual coupling induced by the parametric modulation. Furthermore, the proof of concept of the proposed tuning mechanism is validated on a DC electric field sensor with enhanced sensitivity. The nonlinear parametrically driven sensor exhibits two orders of magnitude sensitivity boost while maintaining a broad measurement range. While our investigation focuses on coupled microresonator systems modeled within a classical framework, the observed dynamics and the simulation extend to the advancements of other cognate fields, such as optomechanics and two-level systems.

Introduction

Coupled resonator structures have attracted significant attention in the field of micro-electromechanical systems[1–3] (MEMS). One of the key approaches to achieving ultra-high sensitivity or an extended measurement range in MEMS sensing is by leveraging the principle of vibration mode localization in weakly coupled resonators[4–6]. In a symmetric system, any perturbation caused by external physical influences leads to a substantial shift in mode shape amplitudes. The amplitude ratio (AR) between two resonators serves as an indicator of the perturbation magnitude, with sensitivity in the linear regime being inversely proportional to the system's coupling strength[6]. This coupling can be realized mechanically, through connecting beams, or via electrostatic forces[7].

In recent years, the introduction of an additional parametric pump has been proposed to enhance sensitivity further and broaden the operational range[8–11]. By applying an electrical pump signal at a frequency corresponding to either the sum or difference of two mechanical modal frequencies—referred to as blue-or-red-sideband excitation—energy transfer between modes can be dynamically controlled[12–17]. Dual-frequency excitation enables tunable mode interactions, which have been previously explored for their potential in sensing applications[18–20]. Prior research has demonstrated the fundamental behavior of parametrically excited electromechanical systems and their associated performance benefits.

Correspondence: Xiaolong Wen (xiaolongwen@ustb.edu.cn) or
Ashwin Seshia (aas41@cam.ac.uk)
[1]School of Mathematics and Physics, Beijing Weak Magnetic Testing and Applied Engineering Technology Research Center, University of Science and Technology Beijing, Beijing, China
[2]Nanoscience Centre, Department of Engineering, University of Cambridge, Cambridge, UK
Full list of author information is available at the end of the article

As device dimensions continue to shrink, nonlinear effects are evident in MEMS devices[4,21–25]. For parametrically modulated coupled resonators, previous studies have primarily focused on employing linear resonator models[15,18,19]. Those that do consider nonlinearities, on the other hand, neglect crucial characteristics, such as the effect of the intra-modal coupling interactions in a parametrically modulated system[14]. As a result, their predictions deviate from what would be expected in such systems with strong nonlinear interactions. For instance, the phenomenon of mode splitting induced by strong parametric modulation in weakly coupled nonlinear resonator systems remains to be thoroughly investigated. Thereafter, motivated by experimental observations where nonlinear effects due to spring hardening/softening are evident, a framework that incorporates such behavior, together with intra-modal and inter-modal coupling is essential. Even though previous work has separately accounted for other nonlinear characteristics, such as nonlinear modal interactions[26–28] and dynamic-range-and-frequency-stability improvements[4,29] in parametrically driven resonators, the interconnection of these phenomena within the same model remains of interest.

In this work, we investigate the nonlinear dynamics of weakly coupled double-ended tuning fork (DETF) microresonators[30] and demonstrate a mechanism to tune coherent energy transfer under strong red-sideband parametric modulation. We explore third-order mechanical nonlinearities and bistability effects induced by appropriate parametric pumping and driving voltages. A comprehensive theoretical framework that fully incorporates nonlinear modal coupling and energy transfer strategies is developed. Numerical results are provided to complement the experimental results and assess the capabilities of the proposed approach. Finally, we configure the MEMS resonator as a DC electric field sensor to demonstrate the enhanced performance achievable when operating in the nonlinear regime while controlling the coherent energy transfer. It is seen that the DETF electric field sensor based on the traditional mode localized-sensing mechanism, enables wide-range electric field strength detection while compromising the sensitivity[30]. The red-sideband approach employed within the same device demonstraes an option to enhance the sensitivity while retaining the measurement range[12,16].

Results

Coupled MEMS DETF resonators in the nonlinear regime

This experimental investigation utilizes a coupled MEMS resonator system comprising DETFs (Fig. 1a; see also Supplementary Section S2 for details of the testing rig and electrical interfaces). The interaction between two of the in-plane oscillation modes (denoted as Mode 1 and Mode 2) is studied (Fig. 1b). The system is composed of two mechanically coupled DETFs, which are individually supported by the T-shape anchoring (Fig. 1c). The dimension of each beam in a given DETF system is $300\,\mu\text{m}(\text{length}) \times 3\,\mu\text{m}(\text{width}) \times 25\,\mu\text{m}(\text{thickness})$. The surrounding electrodes in the optical microscopic diagram are used for input excitation, output sensing, tuning, and input perturbation (see Supplementary Fig. S2.1.2). The resonator body is biased with a DC voltage of 25 V for capacitive sensing. A harmonic excitation signal V_{AC} at $\omega_d \approx \omega_1$ is applied to resonator 1 (Res. 1). In addition to the AC drive, a parametric pump signal at ω_p is applied to the electrode for Res. 2 for coherent control. The effect of the perturbation in the sensing mechanism and the detailed post-amplification circuitry are discussed in Supplementary Information Sections S1.3 and S2.1. The modes we used in this study are the combined in-phase and out-of-phase modes, respectively (see Supplementary Fig. S1,.2.1). Modes 1 and 2 are located at $\omega_1 = 104.338\,\text{kHz}$ and $\omega_2 = 105.590\,\text{kHz}$, where Mode 1 is directly excited and Mode 2 is triggered through the interaction from the parametric modulation. Owing to the geometry of the DETF design, the two modes experience strong Duffing hardening effects when directly excited.

The development of the frequency response spectra of the two modes is presented in Fig. 1b. The curves are measured without the parametric excitation signals applied. The figures only record the amplitudes of resonator 1 (through CH1 in Fig. 1a) subjected to different excitation intensities.

Dynamic coupling between the mechanical modes and the Stokes and anti-Stokes sidebands

The experiments are conducted on the weakly-coupled mechanical resonator system (see Supplementary Figs. S2.1.1, S2.1.2, and Method section for full testing rig description). The MEMS chip is placed in a customized vacuum chamber to achieve low-damping conditions (with a quality factor of 31300 at 1 Pa under linear operation). The signals are amplified by a cascade two-stage amplifier using ADA4817-1 with an overall gain of 160 MV/A (See Supplementary Section S2 for detailed circuit parameters). The system is characterized by linear responses with varying pump frequency within $\Delta\omega \pm 40\,\text{Hz}$ and strength from 0 to 1 V (Fig. 2a–f), where $\Delta\omega = \omega_2 - \omega_1$. The two input harmonics interact with each other to introduce two additional frequency components at $\omega_d \pm \omega_p$. For the proposed excitation scheme, one of the sidebands is located near the untriggered Mode 2 as $\omega_1 + \omega_p \approx \omega_2$, namely anti-Stokes sideband, as the sideband located on the right-hand-side of the fundamental frequency ω_1. Correspondingly, symmetrical sidebands are also located at $\omega_1 - \omega_p$, which is the Stokes sideband of Mode 1. There are four first-order sidebands, each corresponds to the Stokes and anti-Stokes sideband for Mode 1 and 2 (see Supplementary Section

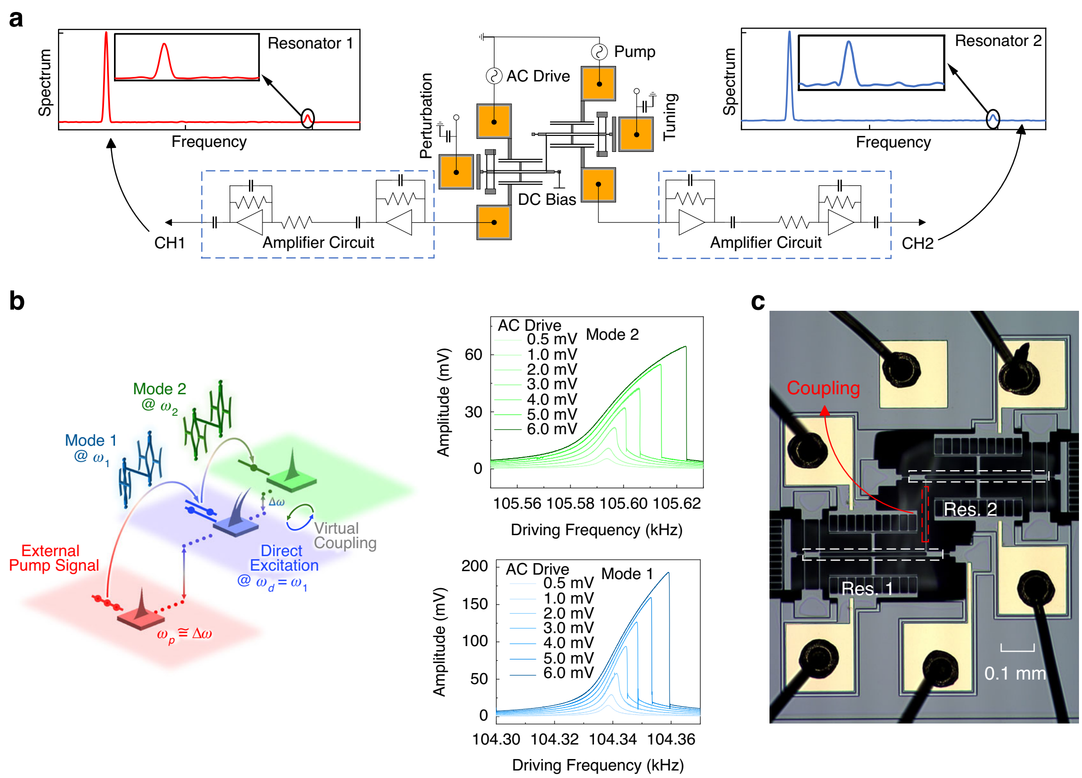

Fig. 1 The schematic overview of the phonon-cavity system using the MEMS resonator-based testing platform. a The schematic view of the weakly coupled tuning fork resonators and the simplified measurement circuit; the AC drive signal at ω_1 and Pump signal at ω_p are generated using the Lock-in Amplifier (LIA); the amplitude of resonator 1 is measured at ω_1, and the amplitude of resonator 2 is measured at $\omega_1 + \omega_p$ using a Keysight signal analyzer. **b** The schematic diagram of the mechanism for the parametric pump applied in the nonlinear regime of the coupled resonator system. Each frequency stage and the corresponding mode shapes, along with the energy transfer routes are presented in the figure. The curved-and-split shape of Mode 1 corresponds to the mode-splitting of the mechanical mode at this frequency, measured at Res. 1. The indirectly triggered Mode 2 (green) is also measured on Res. 1. The nonlinear backbone curve under the forward frequency sweep of each mode is illustrated on the right-hand side without the parametric modulation. **c** A false-color optical image of the MEMS structure for investigation. The layer thickness is 25 μm and the chip is fabricated using a silicon-on-insulator MEMS process

S3,.2.4 for theoretical derivations). When the pumping frequency approaches the difference between the two modal frequencies, the anti-Stokes sideband triggers the resonance of Mode 2. During the process, a greater proportion of energy is transferred to the indirectly excited Mode 2. Simultaneously, due to the presence of a resonant peak at ω_2, a new pair of frequencies at $\omega_2 \pm \omega_p$ also participates in dynamic behaviors. The Stokes sideband of Mode 2 at $\omega_2 - \omega_p$ is located at the modal frequency of Mode 1. Despite the bidirectional development of the sidebands, only the anti-Stokes sideband of Mode 1 induces oscillation at the frequency of Mode 2, whereas the Stokes sideband of Mode 2 introduces a term at the Mode 1 frequency. The results are most significant when the pump frequency is close to $\Delta\omega$. In this circumstance, the developed sidebands exhibit the highest amplitudes owing to resonance with the mechanical modes.

The dynamic energy transfer scheme leads to two unique phenomena, viz. mode splitting and sideband generation, which are the signatures of parametric coupling. The mode-splitting phenomenon is caused by the strong virtual coupling between Mode 1 and the Stokes sideband of Mode 2. The process is similar to the mechanically coupled systems, except for the dynamic coupling introduced by the parametric modulation signal. The intensity of the virtual coupling governs the extent of mode splitting. For a stronger pump intensity, the magnitude of the sidebands is inherently larger, leading to a stronger energy transfer between the modes and hence a more significant virtual coupling. The phenomenon is further validated in the later experiment section, where the sideband amplitude is proportional to the pump intensity. As a result, the coupled model amplitudes reflect on different pump strengths (Mode 1 exhibits 20.5 mV peak for 0.1 V pump, 14.7 mV coupled peaks for 0.5 V pump and 13.1 mV coupled peaks for 0.9 V pump voltages). In the theoretical modeling section, it is also shown that the amplitudes of the sidebands are

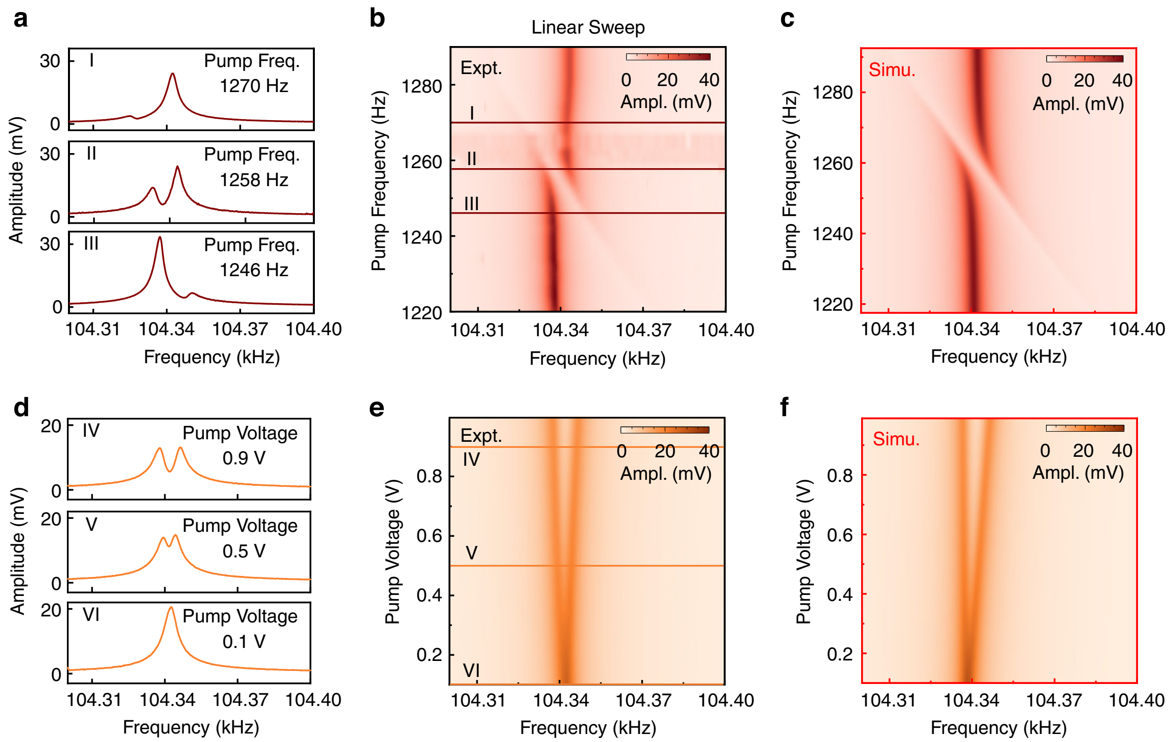

Fig. 2 The experimental results and the numerical simulations of the weakly-coupled resonator system under parametric modulation in the linear regime. a The three frequency response spectra from the amplitude of Res. 1 around the Mode 1 frequencies under different pump frequencies. The pump frequencies are selected so that the Stokes sideband of Mode 2 are located on the left, around, and on the right of the mechanical Mode 1. **b** The 2D rendered heatmap from multiple driving frequency sweeps with different frequencies of pumping signals. The discrete samples are rendered automatically by OriginLab. The locations of the three slices in (**a**) are labeled in the heatmap. **c** The corresponding heatmap obtained from the numerical simulation. The color scales and ranges of sweeps are identical to the experimental results. **d**–**f** A similar set of figures where the y-axes are the voltage of the pump signals. The color scales are identical to the previous heatmaps while orange is used for clarity

proportional to the intra-or-inter model coupling coefficients (see Supplementary Section S3.2.4). The coefficients are only proportional to the pump signal amplitude for a fixed structure with a given driving amplitude.

The experimental results in Fig. 2 match the above-mentioned explanations. The Stokes sideband of Mode 2 is always located at $\omega_2 - \omega_p$ (Fig. 2a, b). However, it is only visible when $\omega_p \approx \Delta\omega$, owing to the resonance amplification from the mechanical modes. Meanwhile, when the Stokes sideband of Mode 2 approaches ω_1, the intrinsic mechanical mode splits into two eigenmodes (see response curve II in Fig. 2a). The energy is distributed to each split mode, which is reflected in their reduced amplitudes compared to the uncoupled Mode 1 in curves I and III.

The coupling strength is also associated with the pump signal intensity (see Fig. 2d, e). The parametric excitation frequency $\omega_p = \Delta\omega$ is fixed at the difference between modal frequencies and hence the split modes are symmetrical. As the pump voltage increases, the frequency difference between the hybridized eigenmodes (generated by the coupling between Mode 1 and the Stokes sideband of Mode 2) increases accordingly, demonstrating a stronger virtual coupling. This indicates a stronger virtual coupling between the Stokes sideband and the mechanical Mode 1 explained before.

Dynamic behavior in the nonlinear regime

The system is driven by an increased AC driving voltage, leading to a strong nonlinear response. The frequency response curves of the spring-hardened system show a clear distinction between the forward and reverse sweep (see Fig. 3b, h, where each pair of graphs shares the same color legend). Since the nonlinear dynamics is governed by a hardening behavior, the forward sweep shows a greater amplitude and bandwidth compared to the reverse sweep results (see Fig. 3b, h). The half-amplitude bandwidth of Mode 1 for forward sweep, 8.81 Hz, is 35% larger than that for the reverse sweep at 6.55 Hz (see slices I and VII in Fig. 3a, g). Overall, the amplitude of the nonlinear responses is about three times higher than that of the linear operations. This matches the driving amplitude, where the AC drive intensities for the linear and nonlinear tests are 1 mV and 3 mV respectively.

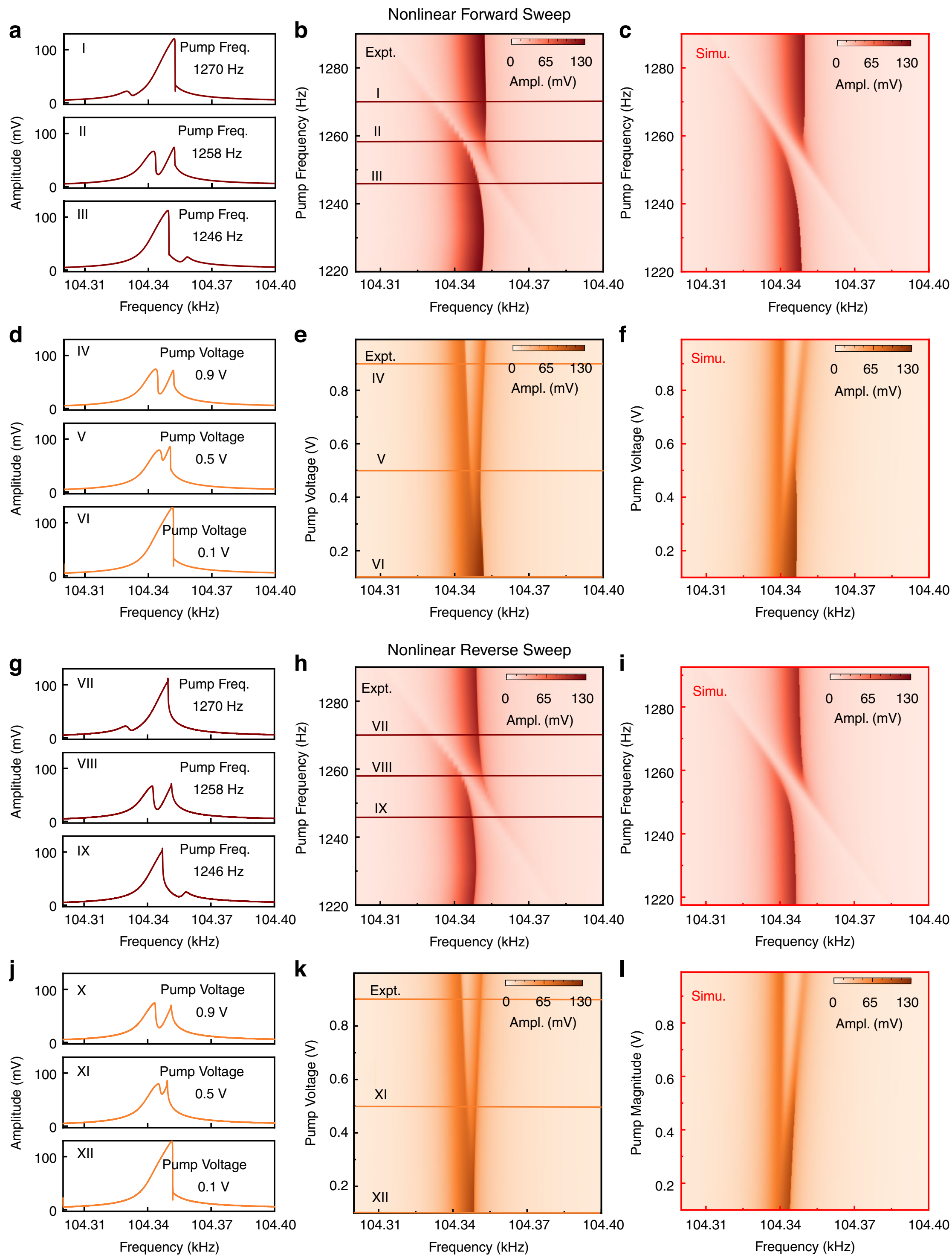

Fig. 3 The experimental results and the numerical simulations of the weakly-coupled resonator system under parametric modulation in the nonlinear regime. a The three forward frequency response spectra from the amplitude of Res. 1 around the Mode 1 frequencies under different pump frequencies. The pump frequencies are selected so that the Stokes sideband of Mode 2 is located on the left, around, and on the right of the mechanical Mode 1. **b** The 2D rendered heatmap from multiple forward driving frequency sweeps with different frequencies of pumping signals. The discrete samples are rendered automatically by OriginLab. The locations of the three slices in (**a**) are labeled in the heatmap. **c** The corresponding heatmap obtained from the numerical simulation. The color scales and ranges of sweeps are identical to the experimental results. **d**–**f** A similar set of figures where the y-axes are the voltage of the pump signals. The color scales are identical to the previous heatmaps while orange is used for clarity. **g**–**l** A similar set of experimental and simulated figures where the amplitudes are obtained via reverse frequency sweeps

Despite higher amplitude and wider bandwidth, the 2D heatmaps with varying pump frequencies show a similar shape compared to the previous linear tests. In particular, the amplitude of the nonlinear peaks is proportional to the pump frequency, whereas the frequency of the bifurcation point of Mode 1 is shifted by 9 Hz to the right with an AC drive of 3 mV (see Fig. 1b). The Duffing nonlinearity induces sharp amplitude drops at the high-frequency bifurcation points. The split modes also exhibit nonlinearity but with lower amplitudes (see slices in Fig. 3a, g). Interestingly, owing to the frequency difference between the bifurcation points of nonlinear spectra, the split modes are symmetrical in nonlinear sweeps but noticeably asymmetrical in linear operation for the same pump frequency $\omega_p = 1258\,\text{Hz}$ (Fig. 2a II compared to Fig. 3a II). For the linear sweeps, the optimal pump frequency $\omega_{p,linear} = \Delta\omega = 1252\,\text{Hz}$ which leads to symmetrical mode-splitting. The corresponding optimal pump frequency value is 1258 Hz in the nonlinear scenario.

In particular, when the pump frequency $\omega_p < \Delta\omega$ or $\omega_p > \Delta\omega$, the mechanical peak remains nonlinear, whereas the Stokes sideband response appears to be linear and with a smaller amplitude; When $\omega_p \approx \Delta\omega$, both peaks exhibit nonlinear effects. The transition of the sideband toward nonlinearity is shown along the diagonal asymptotes in the heatmap (Fig. 3b, h). As the frequency approaches $\Delta\omega$, nonlinearity in the Stokes sideband starts to develop, and the falling edge emerges until the strongest mode-splitting occurs. The process is then reversed when the pump frequency leaves the bandwidth of the mechanical Mode 1, similar to the linear responses.

The variation under different pump signals is also investigated using the same range of pump intensities as the linear experiments (Fig. 3d, e, j, k). The frequency differences of the split modes resemble those in the linear scenario under the same pump strength. This justifies the extent of mode-splitting, and hence, the virtual modal coupling is dominated by the pump signal characteristics instead of the intrinsic properties of the resonators for both linear and nonlinear operation. Interestingly, as the virtual coupling strength increases from zero, the extent of nonlinearity decreases until the split eigenmodes no longer overlap. Quantitatively, the eigenmodes split when the pump voltage exceeds 0.4 V, for both linear and nonlinear tests. The resonant amplitude of the forward-sweep frequency responses around ω_1 decreases as the coupling strength increases (Mode 1 exhibits 128.8 mV peak for 0.1 V pump, 86.0 mV coupled peaks for 0.5 V pump, and 71.9 mV coupled peaks for 0.9 V pump voltages). The Duffing nonlinearity is more pronounced when the modal amplitude is large. Therefore, since the virtual coupling splits the energy of the mechanical mode into two hybridized eigenmodes due to mode interactions, the Duffing nonlinearity becomes no longer observable in each split frequency sweep peak. Without parametric modulation, the Mode 1 amplitudes from forward and reverse sweeps are 120.7 mV and 107.2 mV, respectively. With strong virtual coupling, the reverse-sweep response does not show a significant difference in amplitudes compared to the forward sweeps (the average coupled peak amplitude from the reverse sweep is 71.2 mV, similar to 71.9 mV in the forward responses).

Modeling

The 2-degree-of-freedom (2-DOF) resonant system could be described by the following equation (see Supplementary Information Section S3.2.1):

$$\ddot{x}_1 + \gamma\dot{x}_1 + [\omega_1^2 + \Gamma_1\cos(\omega_p t)]x_1 + \Lambda\cos(\omega_p t)x_2 + \mu x_1^3 = F\cos(\omega_d t), \ddot{x}_2 + \gamma\dot{x}_2 + [\omega_2^2 + \Gamma_2\cos(\omega_p t)]x_2 + \Lambda\cos(\omega_p t)x_1 = 0 \quad (1)$$

Where $x_{1,2}$ are the modal displacements at resonance, $\omega_{1,2}$ are the corresponding natural frequencies, γ is the energy dissipation rate and μ is the hardening nonlinear coefficient. It is assumed that only Mode 1 exhibits nonlinearity since the resonance at Mode 2 is triggered by the frequency interactions at a lower amplitude compared to the directly excited resonance. The harmonic driving force $F\cos(\omega_d t)$ is only applied to Mode 1, where F is the dimensionless driving amplitude and ω_d is the driving frequency. In addition, the intra-modal coupling coefficients $\Gamma_{1,2}$ and the homogeneous inter-modal coupling coefficient Λ are the dimensionless parameters generated through the decoupling process. The two parameters each correspond to the virtual coupling between the Stokes and anti-Stokes sidebands and the mechanical mode. Both parameters are proven to be proportional to the pump strength (see Supplementary Section S3.2.3 for detailed calculations using the multiple scale method).

The numerical results of Eq. (1) could be obtained through the multiple-scale approximation method[31] (see Supplementary Information Section S3.2 for the full derivation). The amplitude responses are therefore generated by solving the equations of motion at different driving and pump parameter settings. The multiple-scale analysis is conducted up to the first-order slow-changing time variable $O(\varepsilon^1)$, whereas the amplitudes and phases of each mode are assumed to change at that time scale. By extracting the secular terms that oscillate with the frequency of ω_1, we obtain the following coupled differential complex equations:

$$\begin{cases} -j\omega_1 a_1' + \omega_1 a_1 \phi_1' - j\gamma\omega_1 a_1 \\ -(\Gamma_1 a_1 + \Lambda a_2 e^{j((\omega_2-\omega_1)T_0+\phi_2-\phi_1)})e^{j\omega_p T_0} \\ -\frac{3}{8}\mu a_1^3 + F e^{j(\omega_d T_0 - \omega_1 T_0 - \phi_1)} = 0 \\ -j\omega_2 a_2' + \omega_2 a_2 \phi_2' - j\gamma\omega_2 a_2 \\ -(\Gamma_2 a_2 + \Lambda a_1 e^{j((\omega_1-\omega_2)T_0+\phi_1-\phi_2)})e^{j\omega_p T_0} = 0 \end{cases} \tag{2}$$

Where $T_0 = t$ is the normal time scale and $T_1 = \varepsilon T_0$ is the slowly changing time since the dimensionless perturbation ε is small. $a_i, \phi_i, i = 1, 2$ are the slowly varying amplitudes and phases of each mode relative to the driving signal at the time scale T_1 and a_i', ϕ_i' are the derivatives with respect to T_1. The resulting equations for the secular terms could not be simplified using the previously reported method by neglecting the intra-model coupling terms Γ_i.The response of each mode is subjected to two harmonic excitations with distinctive frequencies caused by the interaction of the drive and pump signals. The simplification is valid for low-intensity pump signals, where the phenomenon of mode-splitting could be negligible. However, the intra-modal coupling coefficient contributes significantly to the dynamic behavior in our weakly coupled system. We therefore introduce a novel detuning method by neglecting the influence of the pump frequency on the amplitude of fundamental modes since $\omega_p \ll \omega_1$. However, the rate of change of the detuned parameters is retained as the frequency of parametric pump governs the locations of the sidebands. Hence the second detuned phase $\theta_2 = (\sigma_d + \sigma_p)T_1 + \phi_2$, where σ_d and σ_p are the detuning variables for the driving and pump signals near ω_1 and $\Delta\omega$ respectively, and ϕ_2 is the phase of Mode 2 relative to the harmonic excitation. The detuned phase θ_2 for the second mode considers both the detuned variable for the driving frequency and the pump frequency despite $\omega_p \ll \omega_d$. This approach ensures that the influence of the change in pump frequency can be investigated despite its small magnitude. The steady-state amplitude response of each mode $a_{1,2}$ could be obtained by solving the Supplementary Eq. (S3.2.30):

$$\begin{cases} \omega_1 a_1 \sigma_d - \Gamma_1 a_1 - \Lambda a_2 \cos(\theta_1 - \theta_2) - \mu\frac{3}{8}a_1^3 + F\cos(\theta_1) = 0 \\ -\gamma\omega_1 a_1 - \Lambda a_2 \sin(\theta_1 - \theta_2) + F\sin(\theta_1) = 0 \\ \omega_2 a_2(\sigma_d + \sigma_p) - \Gamma_2 a_2 - \Lambda a_1 \cos(\theta_2 - \theta_1) = 0 \\ -\gamma\omega_2 a_2 - \Lambda a_1 \sin(\theta_2 - \theta_1) = 0 \end{cases}$$

where the detailed generation and explanations of the detuning parameters are introduced in the Supplementary Information. The parameters for numerical simulation are fitted to the experimental data using the measured frequencies and amplitudes (the parameters are listed in Supplementary Table S3.1).

The experimentally measured heatmaps and the simulation results are plotted in pairs for theory validation (see Fig. 2 for linear operation, Fig. 3 for nonlinear operation). The simulated results exhibit all the discussed phenomena. The general shape of each pair of plots is also similar, except for the slight frequency shift introduced by the temperature change during the experiment. In particular, the sudden changes at the bifurcation points and the nonlinear mode-splitting phenomenon are presented as ω_p approaches $\Delta\omega$, and the extent of mode splitting is also proportional to the pump signal intensity V_p as expected. The evolution of this unique shape could be explained by manipulating the simulation parameters and their corresponding responses. During the frequency sweep, the resonance first rises along the upper branch of the spring-hardened Duffing oscillation response before falling to another stable branch with a lower amplitude. Meanwhile, when $\omega_p \approx \Delta\omega$, the trough from between the split modes may overlap with the drop from nonlinear oscillation, leading to an earlier sharp edge of the lower-frequency hybridized eigenmode. The Stokes sideband, through simulation, acts as a small linear peak located at a frequency of $\omega_2 - \omega_p$. As the Stokes sideband approaches the mechanical nonlinear peak, energy is transferred to the sideband from Mode 1 (Fig. 1b). The magnitude of the sideband is therefore increased. In addition, the amplitudes of the sidebands are mathematically proven to be proportional to the modal coupling coefficients[32], and hence the parametric pump intensity V_p. The reverse frequency response also exhibits a similar pattern, except for the different stable branches and bifurcation-point responses as explored in the experiment section.

The sidebands play essential roles in such a parametrically modulated weakly-coupled resonator system. Previous work has demonstrated the potential of sensors based on the phenomenon of mode-localization in high-sensitivity detection[33]. The sensitivity of this mechanism is inversely proportional to the coupling stiffness (see Supplementary Section S1.3). In our system with parametric excitation, the dynamic coupling between the mechanical mode and the sidebands is suitable for this application. When the $\omega_p \approx \Delta\omega$, the anti-Stokes sideband with a frequency of $\omega_1 + \omega_p$ appears near Mode 2 (the coupling process is presented in green in Fig. 4a, b). In this process, the virtual coupling strength is controllable by the magnitude of the pump signal, hence achieving a manipulable AR sensitivity as suggested before. According to the coupling mechanism, the amplitude ratio (AR) between Mode 1 of Res. 1 and the anti-Stokes sideband measured at Res. 2 could therefore reflect the amount of stiffness perturbation exerted onto Res. 1. Since the resonators are coupled together, each mode shape involves oscillation of both DETF beams, and the measurement electrodes are selected as in Fig. 1a. The

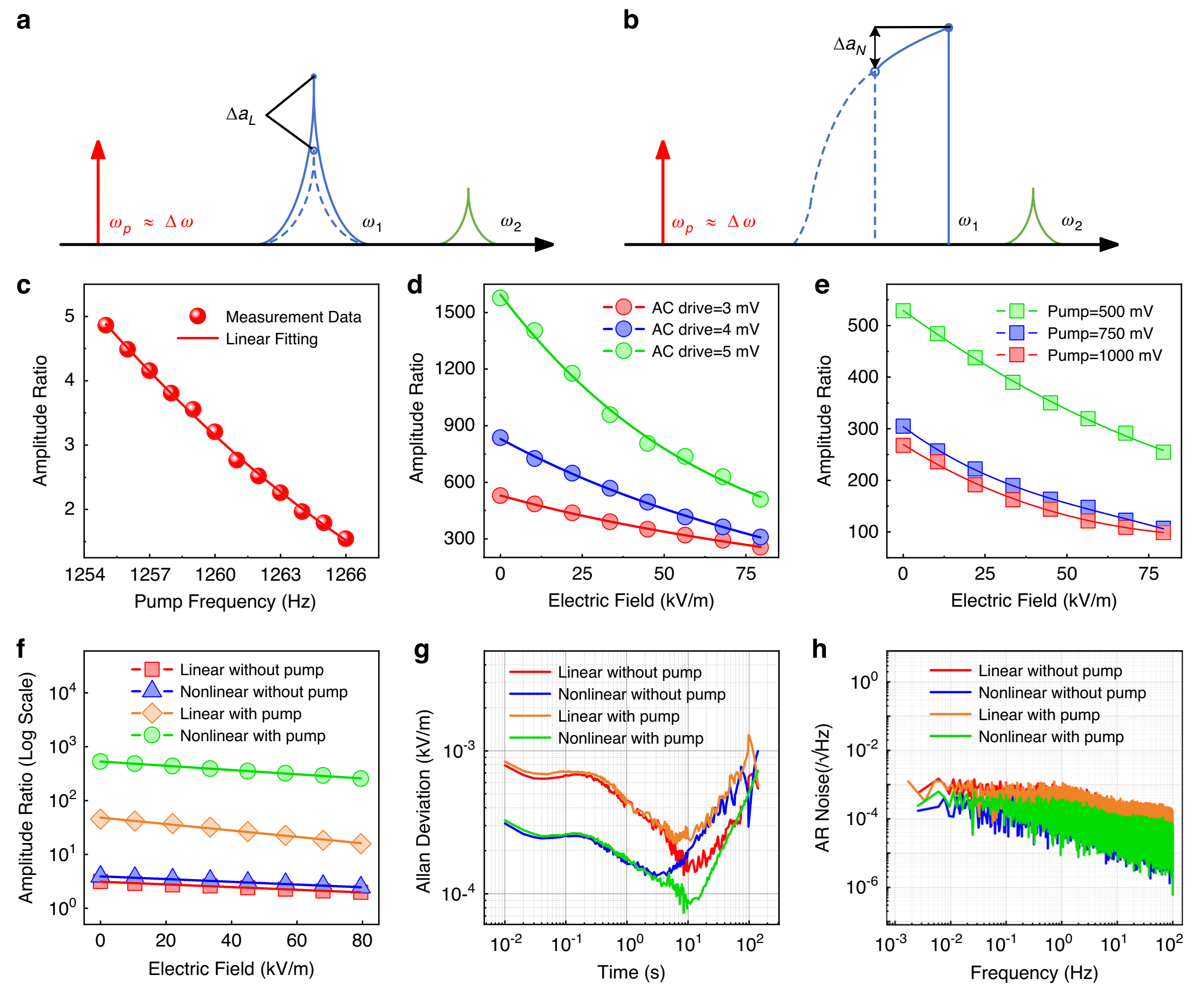

Fig. 4 Performance optimization of mode localization sensing in a nonlinear coupled resonant system utilizing parametric pump. a, **b** The expected frequency spectra of the system under fixed frequency driving for linear operation and nonlinear operations. **c** The operating point of a mechanically coupled system can be adjusted by tuning the parametric pump frequency ω_p. The unperturbed AR varies linearly to the pumping frequency. The AR is the amplitude ratio of the two resonators' mechanical Mode 1. **d** The amplitude ratio (AR) sensitivity is compared under different AC driving voltages ($V_{AC} = 3, 4, 5$ mV) with a fixed pump voltage ($V_p = 500\, mV$). **e** The AR sensitivity is compared under different pump voltages ($V_p = 500, 750, 1000$ mV) with a fixed AC driving voltage ($V_{AC} = 3\, mV$). **f** The comparison of the AR sensitivities in linear and nonlinear regimes, with and without parametric pump. The slopes of the fitted line indicate the sensitivities. **g** The comparison of the Allan deviation in linear and nonlinear regimes, with and without parametric pump. **h** The comparison of the AR noise in linear and nonlinear regimes, with and without a parametric pump

perturbation is intrinsically induced by the target physical quantity through structural design[34–36] (electric field, acceleration through a proof mass, thermal stress, etc.).

The sensitivity enhancement due to nonlinearity for a parametrically driven sensor is more significant. In both the linear and nonlinear regime, the energy from the linear Mode 1 is transferred to the anti-Stokes sideband around ω_2 (Fig. 4). However, the amount of energy transferred, hence the amplitude of the sideband and induced resonance of Mode 2, are proportional to the pump intensity V_p and the inter-and-intra-modal coupling coefficients. Therefore, for a known mechanical structure and fixed pump strength, the AR is only dominated by Mode 1 amplitude. Despite slight amplitude variation introduced by nonlinearity, the amplitudes of Mode 1 for both resonators are proportional to the AC drive signal amplitude, and hence the AR sensitivity. On the contrary, in the physically coupled systems, an increased driving intensity leads to the amplitude amplification of both resonators, which indicates a minimal enhancement of the AR sensitivity. An ultra-low mechanical or electrostatic coupling could resolve it, but a minimum strength limits the sensitivity enhancement, below which the energy transfer between resonators is fully dissipated by material damping. Besides, a weak physical coupling could result in modal overlap, complicating the measurements in such a mode-localized design[37].

Mode-localized electric field sensor based on nonlinear oscillation and parametric excitation

The design and driving mechanism are tested through the testing rigs described in Supplementary Figs. S2.1.1, S2,.1.2. The amplitudes of the mechanical Mode 1 and the anti-Stokes sideband are read simultaneously using the output spectrum of the Keysight Signal Analyzer for multi-frequency readout rather than the frequency-sweep spectra. The enhancement of the sensing performance is tested using an external electric field and a metal plate acting as a charge collector. Resonator 1 is driven with the fundamental frequency $\omega_d = \omega_1$ and the pump signal $\omega_p \approx \Delta\omega$ simultaneously. The electrostatic force exerts a longitudinal stress on the DETF (see Supplementary Information Section S2 for detailed testing methods). The MEMS resonator is placed in a 1 Pa environment to eliminate air acoustic damping. The unperturbed AR of the two resonator amplitudes at Mode 1 could be linearly adjusted by the pump frequency (Fig. 4c). The pump signal effectively exerts an external perturbation to Res. 2, leading to slight asymmetry and mode localization in the system. Using this method, we could adjust the operation point of the mode-localized sensor under unperturbed situations.

The sensor performance readings are obtained from the spectra of the Keysight Signal Analyzer. Due to the fixed-frequency excitation, the split modes could not be observed in the frequency domain (See spectra in Fig. 1a). This is attributed to the fact that the spectra are obtained from the Fourier transform of the time-domain oscillation instead of the frequency sweep, so only the driving frequencies and the generated sidebands are recorded. The pump frequency in the remainder of this experiment is fixed to $\omega_p = 1258\,\mathrm{Hz}$ for the best performance. The AR sensitivity curves in the nonlinear regime, subjected to different AC driving voltages, are plotted in Fig. 4d, where the pump voltage $V_p = 500\,\mathrm{mV}$. The electric field is used as the source of perturbation up to 80 kV/m, beyond which the sideband is submerged in the noise floor. The perturbation changes the mechanical stiffness of Res. 1, leading to a change in the inter- and intra-modal coupling and, further, the amplitude of the sideband. Simultaneously, the energy is localized to the mechanical Mode 1, leading to the sensitivity enhancement under different AC driving strengths (3.4/(kV/m) for 3 mV drive, 6.5/(kV/m) for 4 mV drive, 13.4/(kV/m) for 5 mV drive). The influence of pump intensity on sensitivity is also investigated with a fixed AC drive $V_{AC} = 3\mathrm{mV}$. As expected, the pump strength influences the amplitude of the sideband, and hence inversely influences the AR. The sensitivity is therefore inversely proportional to the pumping voltage (3.4/(kV/m) for 500 mV pump, 2.4/(kV/m) for 750 mV pump, 2.1/(kV/m) for 1000 mV pump) as the resonant behavior of Mode 1 is unchanged by the pump. However, a small sideband leads to a low signal-to-noise ratio, hence the selection of the pump strength should consider the trade-off between the noise performance and the sensitivity.

The performance advancement of the mode-localized sensor with nonlinearity and parametric modulation is now compared in Fig. 4f–h. For all sets of experiments, the linear driving voltage is 1 mV and the nonlinear driving voltage is 3 mV. The pump strength is 500 mV. The AR sensitivity curves are plotted at the log scale for their distinctive amplitudes (Fig. 4f). The AR sensitivities S_{AR} are measured as the slope of the linear-fitted curves in the figure. The AR sensitivity of the linear operation is increased by 28 times due to the addition of parametric modulation, from 0.014 to 0.39/(kV/m). Similarly, parametric excitation boosts the nonlinear sensitivity by 200 times, from 0.017 to 3.4/(kV/m). The parametric pump method successfully increases the sensitivity while only compromising the measurement range by a factor of 2.5 (See ref. [30] for performances of the previously reported sensor using the same structure). Meanwhile, nonlinearity enhances the sensitivity by 1.2 times for the system without parametric modulation. The value rises to 8.7 with parametric excitation. The differences match the theoretical model and the experimental results mentioned above.

Other aspects of the electric field sensors are also investigated. The Allan deviation spectra reveal the noise performances and the longer stability of the sensor (Fig. 4g). At a short time cluster, both nonlinearly mitigated solutions exhibit a low noise level compared to the linear operations. For the longer integration times, the system with both nonlinearity and parametric pump exhibits the best stability. Compared to the nonlinear resonators without the pump, the instability decreases from 0.14 to 0.08 V/m because of the large operating AR. However, this improvement is not reflected in the linear sets for intermediate integration times at 10 s (when an increase in the Allan deviation from 0.15 to 0.25 V/m). This is attributed to the noise induced by the pump signals, whereas in the linear operation with low resonant amplitude, the magnitudes of sidebands are easily influenced by any additional noise. Besides, the parametrically modulated system shows better noise performances compared to the traditional mode-localized sensors (see Fig. 4h). The sensor achieves the lowest average noise floor of 0.04 $(\mathrm{V/m})/\sqrt{\mathrm{Hz}}$, with the addition of both nonlinear operation and parametric modulation. The value is improved by 557.5 times compared to the linear sensors with mechanical mode-localization.

Discussion

The experimental results extend the understanding of the parametrically excited coupled-resonator systems with nonlinearity. Interesting phenomena such as side-band generation and mode splitting are explored in nonlinear operation regimes. The controllable virtual coupling between the mechanical Mode 1 and a virtual eigenmode generated through the interaction between the resonator structure and the parametric pumping signal illustrates distinctive characteristics compared to physics-governed coupling. The theoretical derivations and the corresponding simulation program enable better visualization and understanding of further optimization of the system and future study regarding such systems in their nonlinear regimes.

The model also provides insights into other related fields. The energy transfer process resembles the phonon exchange routes in a parametrically manipulated phonon-cavity system. The observed nonlinear mode interactions and coherent energy transfer mechanisms closely resemble phonon dynamics in solid-state quantum systems, where controlled phonon exchange is pivotal for quantum information processing[38], phononic logic[39], and high-precision sensing[14]. In quantum phononics, phonons serve as carriers of quantum information and can be manipulated using parametric excitation similar to the one demonstrated in the study. The controlled mode splitting and nonlinear interactions can be analogized to phonon-mediated quantum state transfer in optomechanical and nanomechanical systems. Advances in cavity optomechanics have shown that phonon-photon interactions enable coherent coupling between mechanical models and quantum states of light, enabling translation between optical and microwave frequencies.

The paper demonstrates the potential of the system for high-performance sensing. The compromise between the broad measurement range and high sensitivity often limits traditional sensors. In previous work, we have demonstrated the potential of this DETF-based weakly coupled resonator to provide a wide electric field sensing range of up to 200 kV/m[30]. The quantity is crucial in fields like atmospheric sensing or high-voltage DC power transmission system monitoring. However, with the parametric pump techniques proposed in this work, we modified the exact same structure into a sensor with a 200-times boost in sensitivity while maintaining a measurement range of 80 kV/m. The same sensing mechanism could be used in accelerometers, gyroscopes, pressure, and mass sensors with remarkable sensitivity and operating range simultaneously.

Methods

The die embedding the MEMS resonator is fixed in a ceramic leadless chip carrier, which is further soldered to a customized PCB for post-amplification and signal input. The PCB is placed in a customized vacuum pump under an ambient room temperature environment. The full testing rig and the detailed testing methods, including the devices, the generation of the electric field, etc. are discussed in detail in Supplementary Information Section S2. The simulation codes are based on Python 3.12 with *Numpy* and *Matplotlib* as basic establishment and visualization packages. *SciPy.optimize* is used for numerical solutions to the nonlinear simultaneous equations.

Acknowledgements

This work was supported by the National Natural Science Foundation of China under Grant 62031025; in part by the National Key Research and Development Program of China under Grant 2024YFF1502300; in part the Defense Industrial Technology Development Program of China under Grant JCKY2022110C013; in part by China Scholarship Council; and in part by an EUR EIPHI Program, Europe, under Contract ANR 17-EURE-0002.

Author details

[1]School of Mathematics and Physics, Beijing Weak Magnetic Testing and Applied Engineering Technology Research Center, University of Science and Technology Beijing, Beijing, China. [2]Nanoscience Centre, Department of Engineering, University of Cambridge, Cambridge, UK. [3]FEMTO-ST Institute, CNRS, Université Marie et Louis Pasteur, Besançon, France

Author contributions

G.W. and S.H. contributed equally to this paper. G.W. conceived the idea under the guidance of X.W. and A.A.S. The structure is designed by X.W., G.W. and S.H. The measurement and data analysis is designed and conducted by G.W. and L.R. The theoretical derivation and numerical simulation is conducted by S.H. under the supervision of N.K. The manuscript is written by S.H., G.W. under the supervision of A.A.S., X.W. and N.K. The project is planned by X.W.

Data availability

The authors declare that all data and codes supporting the findings of this study are included in the paper and its supplementary information files, and are available on request from the corresponding authors. The simulation programs are pushed and committed on https://github.com/sh2147/Parametric_Modulation_Simulation_sh2147.

Competing interests

The authors declare no competing interests.

Supplementary information The online version contains supplementary material available at https://doi.org/10.1038/s41378-025-01059-2.

Received: 18 April 2025 Revised: 2 August 2025 Accepted: 1 September 2025
Published online: 11 November 2025

References

1. Zhang, Z., Zhang, H., Hao, Y. & Chang, H. A review on MEMS silicon resonant accelerometers. *J. Microelectromech. Syst.* **33**, 174–208 (2024).
2. Chang, H. Serial and parallel connections of micromechanical resonators for sensing: theories and applications. *J. Microelectromech. Syst.* **32**, 213–228 (2023).
3. Zhao, C. et al. A review on coupled MEMS resonators for sensing applications utilizing mode localization. *Sens. Actuators A Phys.* **249**, 93–111 (2016).
4. Zhang, H. et al. Mode-localized accelerometer in the nonlinear Duffing regime with 75 ng bias instability and 95 ng/√Hz noise floor. *Microsyst. Nanoeng.* **8**, 17 (2022).

5. Thiruvenkatanathan, P., Yan, J., Woodhouse, J., Aziz, A. & Seshia, A. A. Ultra-sensitive mode-localized mass sensor with electrically tunable parametric sensitivity. *Appl. Phys. Lett.* **96**, 081913 (2010).
6. Wang, L. et al. A novel 3-DoF mode localized BAW resonant mass sensor with high quality factor and resolution. *IEEE Trans. Electron Devices* **71**, 4926–4931 (2024).
7. Pachkawade, V. State-of-the-Art in mode-localized MEMS coupled resonant sensors: a comprehensive review. *IEEE Sens. J.* **21**, 8751–8779 (2021).
8. Faust, T., Rieger, J., Seitner, M. J., Kotthaus, J. P. & Weig, E. M. Coherent control of a classical nanomechanical two-level system. *Nat. Phys.* **9**, 485–488 (2013).
9. Mahboob, I., Nishiguchi, K., Okamoto, H. & Yamaguchi, H. Phonon-cavity electromechanics. *Nat. Phys.* **8**, 387–392 (2012).
10. Okamoto, H. et al. Coherent phonon manipulation in coupled mechanical resonators. *Nat. Phys.* **9**, 480–484 (2013).
11. De Alba, R. et al. Tunable phonon-cavity coupling in graphene membranes. *Nat. Nanotech.* **11**, 741–746 (2016).
12. Wang, Y. et al. A resonant Lorentz-force magnetometer exploiting blue sideband actuation to enhance sensitivity and resolution. *J. Microelectromech. Syst.* **31**, 402–407 (2022).
13. Zhou, X. et al. Dynamic modulation of modal coupling in microelectromechanical gyroscopic ring resonators. *Nat. Commun.* **10**, 4980 (2019).
14. Miao, T. et al. Nonlinearity-mediated digitization and amplification in electromechanical phonon-cavity systems. *Nat. Commun.* **13**, 2352 (2022).
15. Zhang, H. et al. Amplitude-modulated resonant accelerometer employing parametric pump. *Appl. Phys. Lett.* **117**, 163504 (2020).
16. Wang, L. et al. Enhanced mode localization in 2-DoF weakly coupled electrostatic MEMS resonant sensor devices via blue-sideband excitation. *IEEE Trans. Electron Devices* **72**, 1345–1351 (2025).
17. Xu, L. et al. A closed-loop system for resonant MEMS sensors subject to blue-sideband excitation. *J. Microelectromech. Syst.* **31**, 690–699 (2022).
18. Zhao, C. et al. Toward high-resolution inertial sensors employing parametric modulation in coupled micromechanical resonators. *Phys. Rev. Appl.* **12**, 044005 (2019).
19. Wang, B. et al. The dynamic characteristics of a mode-localized resonant accelerometer. *J. Microelectromech. Syst*. 1–9 https://doi.org/10.1109/JMEMS.2025.3541581 (2025).
20. Zhang, H. et al. A mode-localized mems accelerometer in the modal overlap regime employing parametric pump. In *2021 21st International Conference on Solid-State Sensors, Actuators and Microsystems (Transducers)* 108–111 (IEEE, 2021). https://doi.org/10.1109/Transducers50396.2021.9495639.
21. Najar, F. et al. Differential capacitive mass sensing based on mode localization in coupled microbeam arrays. *Mech. Syst. Sig. Process.* **220**, 111648 (2024).
22. Liu, Z. et al. Nonlinearity enhanced mode localization in two coupled MEMS resonators. *Int. J. Mech. Sci.* **271**, 109133 (2024).
23. Lyu, M. et al. Computational investigation of high-order mode localization in electrostatically coupled microbeams with distributed electrodes for high sensitivity mass sensing. *Mech. Syst. Signal Process.* **158**, 107781 (2021).
24. Li, C. et al. On extending signal-to-noise ratio of resonators for a MEMS resonant accelerometers using nonlinearity compensation. *J. Microelectromech. Syst.* **33**, 568–576 (2024).
25. Barbosa, A., Kacem, N. & Bouhaddi, N. Standing solitons tuned by impurities in damped nonlinear lattices under external excitation. *Phys. Rev. Lett.* **133**, 187201 (2024).
26. Li, C., Qiu, B., Yoshioka, Y., Hirakawa, K. & Zhang, Y. Mechanical control of nonlinearity in doubly clamped MEMS beam resonators using preloaded lattice-mismatch strain. *Phys. Rev. Appl.* **19**, 024025 (2023).
27. Bitar, D., Kacem, N. & Bouhaddi, N. Investigation of modal interactions and their effects on the nonlinear dynamics of a periodic coupled pendulums chain. *Int. J. Mech. Sci.* **127**, 130–141 (2017).
28. Westra, H. J. R., Poot, M., Van Der Zant, H. S. J. & Venstra, W. J. Nonlinear modal interactions in clamped-clamped mechanical resonators. *Phys. Rev. Lett.* **105**, 117205 (2010).
29. Lee, J. et al. Electrically tunable single- and few-layer MoS_2 nanoelectromechanical systems with broad dynamic range. *Sci. Adv.* **4**, eaao6653 (2018).
30. Wang, G. et al. A weakly coupled tuning fork MEMS electric field sensor with high resolution and wide measurement range. *J. Microelectromech. Syst.* **34**, 82–91 (2025).
31. Salih, A. *The Method of Multiple Scales* (Department of Aerospace Engineering, 2014).
32. Yang, Q. et al. Asymmetric phononic frequency comb in a rhombic micromechanical resonator. *Appl. Phys. Lett.* **118**, 223502 (2021).
33. Pandit, MN. Towards ultra-high resolution mode-localised MEMS sensors. 2019, https://doi.org/10.17863/CAM.44901.
34. Kang, H., Ruan, B., Hao, Y. & Chang, H. A mode-localized resonant accelerometer with self-temperature drift suppression. *IEEE Sens. J.* **20**, 12154–12165 (2020).
35. Hao, Y. et al. A mode-localized DC electric field sensor. *Sens. Actuators A Phys.* **333**, 113244 (2022).
36. Li, H., Zhang, Z., Zu, L., Hao, Y. & Chang, H. Micromechanical mode-localized electric current sensor. *Microsyst. Nanoeng.* **8**, 42 (2022).
37. Zhang, H. et al. On weakly coupled resonant MEMS transducers operating in the modal overlap regime. *IEEE Trans. Ultrason. Ferroelect, Freq. Contr.* **68**, 1448–1457 (2021).
38. Burgwal, R. & Verhagen, E. Enhanced nonlinear optomechanics in a coupled-mode photonic crystal device. *Nat. Commun.* **14**, 1526 (2023).
39. Huang, J. et al. Dynamic phonon manipulation by optomechanically induced strong coupling between two distinct mechanical resonators. *ACS Photonics* **6**, 1855–1862 (2019).